QUARTERLY JOURNAL OF THE ROYAL METEOROLOGICAL SOCIETY
Q. J. R. Meteorol. Soc. **133**: 479–490 (2007)
Published online in Wiley InterScience
(www.interscience.wiley.com) DOI: 10.1002/qj.28

RMetS
ROYAL METEOROLOGICAL SOCIETY

Towards a new hybrid cumulus parametrization scheme for use in non-hydrostatic weather prediction models

V. Kuell,* A. Gassmann and A. Bott
University of Bonn, Germany

ABSTRACT: Classical mass flux parametrization schemes for cumulus convection generally transport heat and moisture only but do not include a *net* mass transport. This is well justified for large grid spacings comprising the whole convective circulation in the local grid column, such that all convective mass fluxes locally cancel out. A conceptual problem arises for finer grid spacings as used in contemporary numerical weather prediction (NWP) models, when convection becomes *partially resolvable*. This problem can be overcome by the *hybrid* approach presented here. Only updraft and downdraft are parametrized with a net mass transport; the environmental subsidence is treated by the grid-scale equations. The total mass flux in the continuity equation is split into a grid-scale and a subgrid-scale contribution. This parametrization scheme is designed for use in any nonlinear, non-hydrostatic and fully compressible NWP model. We here have chosen the Lokal–Modell (LM) of Deutscher Wetterdienst.

Idealized dry mass lifting experiments (without convective heat transport) demonstrate the feasibility of the hybrid approach. Entrainment causes grid-scale convergence and the detrained air, if set to the environmental temperature, spreads mainly horizontally on the grid. Gravity waves are generated when convection starts and ends. Whereas their amplitude depends on the details of the switching on and off of convection, the stationary state (after about 30 minutes) does not. Four model runs with different grid spacings (3.5 km to 28 km) confirm that the mass exchange between the model grid and the parametrization scheme is independent of the chosen grid spacing. Total mass in a convective circulation cell is conserved to better than 0.1%, but only if the damping layer at the upper boundary of the LM is shifted to above 20 km.

For moist convection (with convective heat transport), a simple cloud model for an updraft has been set up. As the detrained air at the cloud top is colder than the environment, it moves down by about 1 km but then mainly spreads horizontally again over several tens of kilometres as in the dry case without convective heat transport.

The hybrid mass flux approach with both a grid-scale and a subgrid-scale contribution may fill the gap between coarse-grid models (grid spacing > 50 km) with classical parametrization schemes, and very highly resolved explicit convection modelling (with a grid spacing of the order of 100 m). Copyright © 2007 Royal Meteorological Society

KEY WORDS convection; mass transport; mesoscale modelling

Received 29 June 2006; Revised 13 November 2006; Accepted 16 November 2006

1. Introduction

Cumulus convection plays a major role in the energetics and dynamics of atmospheric circulation systems (e.g. Charney and Eliassen, 1964; Manabe and Strickler, 1964; Kuo, 1965). In numerical weather prediction (NWP) models, convection cells are usually parametrized as subgrid processes due to their small horizontal extent compared to the grid spacing. Even with quite fine horizontal grid spacings of around 10 km, mesoscale models are not able to represent convective clouds explicitly; they form updrafts and downdrafts on a scale much larger than found in nature and they generally need saturation at the grid scale, a process which develops rather slowly. Explicitly modelled convective processes thus evolve more slowly and more intensively than expected (Weisman *et al*., 1997). Numerical studies with very highly resolved flows found that meaningful explicit simulations of cumulus convection should be performed with grid spacings of the order of 100 m (Bryan *et al*., 2003). Consequently, a parametrization scheme for convection will remain unavoidable (Molinari, 1993; Bechtold *et al*., 2001).

The main task of a convection parametrization scheme is to restore a convectively unstable layer to stability by convective processes: the vertical redistribution of mass, moisture and energy by the constraint of some equilibrium condition. Essential features of convection are the release of latent heat due to condensation and freezing as well as the production of convective precipitation at the ground. Convective parametrization schemes for mesoscale models consist of three main parts: the triggering mechanism, the cloud model and the closure assumption. The final state of the atmosphere is either predefined (adjustment schemes, e.g. Kuo, 1965; Manabe *et al*., 1965; Kurihara, 1973; Betts, 1986) or derived from a mass flux calculation of a cloud model (mass flux

* Correspondence to: V. Kuell, Meteorological Institute, University of Bonn, Auf dem Huegel 20, Bonn, D-53121 Germany.
E-mail: vkuell@uni-bonn.de

schemes, e.g. Arakawa and Schubert, 1974; Fritsch and Chappell, 1980; Tiedtke, 1989; Gregory and Rowntree, 1990; Bechtold *et al.*, 2001; Kain, 2003).

Classical mass flux schemes compute convective tendencies of temperature and moisture assuming that there is no net mass transport in the convective grid column. This is well justified for NWP models with large grid spacing, i.e. large compared to the horizontal extent of the circulation caused by a convective cell. In such models the mass fluxes of the updraft, downdraft and environmental subsidence can be assumed to be confined in the local grid column and thus all convective mass fluxes cancel out. Irrespective of the grid spacing, the compensational subsidence in particular has to occur in the same grid column. This problem is stated by Kain and Fritsch (1993).

The assumption of the convective mass fluxes being confined in the local grid column becomes questionable for current NWP models with a horizontal grid spacing of a few kilometres.

In the present paper we develop a mass flux scheme, which overcomes this conceptual problem. Mapes (2003) recalls the fact that the compensating subsidence is generally trapped within the Rossby deformation radius ($\approx$ 1000 km) which is much larger than the grid spacing in a numerical mesoscale model. Thus, parts of the complete convective overturning are resolvable. Kain and Fritsch (1993) suggested as a future objective to exchange mass between the grid scale and subgrid scale by means of convective mass source and sink terms in a grid-scale continuity equation. Shutts (1994) analytically studied the adjustment process due to localized mass sources for a linearized two-dimensional hydrostatic set of equations with the Boussinesq approximation. Gray *et al.* (1998) and Gray (1999) used subgrid mass transfer to analyse the dynamics and energy partitioning in mesoscale convective systems and convectively generated anomalies of potential vorticity (PV) in a non-hydrostatic but anelastic Boussinesq model. Chagnon and Bannon (2005) compare the effects of mass, heat, and momentum injection into a linearized compressible model regarding the partitioning of total energy to several wave types and discuss differences to Boussinesq models.

Compared to these previous studies our approach is designed for use in nonlinear non-hydrostatic and fully compressible models as currently used for NWP and it aims at the development of a cumulus convection scheme. In our scheme the updraft and downdraft still are assumed to be confined in the local grid column due to their small horizontal scale. The environmental subsidence may also cover the surrounding grid columns. Thus, our approach parametrizes a *net* upward mass flux due to updraft and downdraft in the local grid column. The environmental subsidence then becomes a grid-scale phenomenon to be simulated by the grid-scale equations. We call this procedure, which simulates convection *both* by subgrid-scale *and* grid-scale contributions, a *hybrid* convection scheme. The scale of the updraft and downdraft represents a lower limit for the grid spacing of the hosting model, in which our convection scheme can be applied. In contrast to classical schemes, which only pass temperature and moisture tendencies to the grid-scale equations of the hosting model in order to adjust its heat and moisture distribution, our scheme also adjusts the grid-scale mass distribution by passing a density tendency (or pressure tendency depending on the choice of prognostic variables). As the hosting model we here use the Lokal–Modell (LM) of Deutscher Wetterdienst (DWD).

The present paper introduces our approach for a new mass flux scheme and analyses its behaviour in idealized cases to study its dynamic effects. In a subsequent paper this approach will be extended to a full convection parametrization scheme including a complete cloud model, trigger and closure.

The present paper is organized as follows: section 2 gives an overview of the model set-up. Some basics of the LM are introduced and the physics of our mass flux scheme is presented. In section 3 an idealized experiment of dry convective mass transport is analysed, which is extended to moist convection in section 4.

2. Model set-up

2.1. Hosting model

Our mass flux scheme is designed for use in a nonlinear non-hydrostatic and fully compressible NWP model. For the numerical experiments presented in this paper, we have chosen the LM of DWD as the hosting model. The LM is based on the following set of (averaged) primitive equations (cf. (3.30)–(3.33) of Doms and Schättler 2002, hereinafter abbreviated as DS):

$$\rho \frac{\mathrm{d}\mathbf{v}}{\mathrm{d}t} = -\nabla p + \rho \mathbf{g} - 2\boldsymbol{\Omega} \times (\rho \mathbf{v}) - \nabla \cdot \mathcal{T} \tag{1}$$

$$\frac{\mathrm{d}\rho}{\mathrm{d}t} = -\rho \nabla \cdot \mathbf{v}, \tag{2}$$

$$\rho \frac{\mathrm{d}q^x}{\mathrm{d}t} = -\nabla \cdot (\mathbf{J}^x + \mathbf{F}^x) + I^x, \tag{3}$$

$$\rho \frac{\mathrm{d}h}{\mathrm{d}t} = -\frac{\mathrm{d}p}{\mathrm{d}t} + B^h - \nabla \cdot (\mathbf{J}^{\mathrm{e}} + \mathbf{F}^h + \mathbf{R}) + \kappa. \tag{4}$$

The following symbols are used:

- $\mathbf{g}$ apparent acceleration vector due to gravity
- h specific enthalpy
- p pressure
- q^x specific content of moisture constituent x, with $x =$ v (vapour), l (liquid), i (ice)
- $\mathbf{v}$ velocity vector
- B^h source term of enthalpy due to buoyant heat and moisture fluxes
- $\mathbf{F}^h$ turbulent flux of enthalpy
- $\mathbf{F}^x$ turbulent flux of moisture constituent x
- I^x sources/sinks of moisture constituent x
- $\mathbf{J}^{\mathrm{e}}$ diffusion flux of internal energy
- $\mathbf{J}^x$ diffusion flux of moisture constituent x

DOI: 10.1002/qj

$\mathbf{R}$ flux density of solar and thermal radiation
$\mathcal{T}$ stress tensor due to viscosity and turbulent flux of momentum
κ kinetic energy dissipation due to viscosity
ρ total density
$\mathbf{\Omega}$ constant angular velocity vector of the Earth's rotation

In the LM, Equations (2) and (4) are transformed to the prognostic variables p and T (temperature). For further details see the LM documentation by DS. The operational version of the LM is run at a horizontal grid spacing of about 7 km. However, the behaviour of our mass flux scheme will also be tested with different grid spacings of the hosting model.

Our mass flux scheme directly calculates convective tendencies of the prognostic variables ρ, h, and q^x. For the coupling to the LM, these tendencies are converted to p, T, and q^x (see appendix). Although at present our scheme is technically designed to be coupled to the LM, it may be easily transferred to any other model with possibly different prognostic variables.

2.2. Convective mass transport

In NWP models with a high spatial resolution of a few kilometres, updraft and downdraft which usually have a small horizontal extent, may still be treated as subgrid-scale processes. However, the environmental subsidence may already cover the neighbour grid columns.

Concerning this problem Kain and Fritsch (1993) suggested: 'In general, a more realistic approach may be to solve for the compensating environmental motions on the resolvable scale by including convective mass source and sink terms in a resolvable scale continuity equation'.

Following this approach, we formulate the convective redistribution of mass starting from the conservation of mass in the hosting model. We define a control volume V which contains the volume of both the convective updraft and downdraft and which is set equal to the local grid column volume. This means that both updraft and downdraft are still assumed to be of subgrid scale, which is essential for our convection scheme.

$$\int_V \left(\frac{\partial \rho}{\partial t} + \nabla \cdot (\rho \mathbf{v}) + \nabla \cdot \mathbf{J}^{\mathrm{m}}_{\mathrm{conv}} \right) \mathrm{d}V = 0. \qquad (5)$$

Here, ρ and $\mathbf{v}$ denote the *grid-scale* density and velocity which means that the product $\rho\mathbf{v}$ represents the *grid-scale* mass flux. The *subgrid-scale* mass flux $\mathbf{J}^{\mathrm{m}}_{\mathrm{conv}}$ accounts for convective mass fluxes which are not resolved by the hosting model. The parametrization scheme which handles this subgrid-scale mass flux has to be mass conservative within the convective grid column:

$$\int_V \left(\nabla \cdot \mathbf{J}^{\mathrm{m}}_{\mathrm{conv}} \right) \mathrm{d}V = 0. \qquad (6)$$

This claim together with Equation (5) ensures also that, on the grid scale, mass is conserved within the convective grid column:

$$\int_V \left(\frac{\partial \rho}{\partial t} + \nabla \cdot (\rho \mathbf{v}) \right) \mathrm{d}V = 0. \qquad (7)$$

In a NWP model the grid columns are usually subdivided by vertical levels into single grid boxes. Then in a *single* grid box mass is no longer a quantity *conserved on the grid scale*, but it is *interchanged* between the grid scale (hosting model) and the subgrid scale (parametrization scheme). Reducing the control volume V in Equation (5) to the minimum value possible in the hosting model (a single grid box) we get the local conservation of total mass:

$$\frac{\partial \rho}{\partial t} + \nabla \cdot (\rho \mathbf{v}) + \nabla \cdot \mathbf{J}^{\mathrm{m}}_{\mathrm{conv}} = 0. \qquad (8)$$

At a particular grid point, the convective density tendency (with subscript conv) to be passed to the hosting model then is

$$\left. \frac{\partial \rho}{\partial t} \right|_{\mathrm{conv}} = -\nabla \cdot \mathbf{J}^{\mathrm{m}}_{\mathrm{conv}} = -\left(\frac{1}{A} \frac{\partial M_{\mathrm{u}}}{\partial z} + \frac{1}{A} \frac{\partial M_{\mathrm{d}}}{\partial z} \right). \qquad (9)$$

Subscripts u and d denote updraft and downdraft quantities respectively and symbols without subscripts denote grid-scale quantities. A denotes the area of the local grid column and M_{u} (M_{d}) is the mass flux in the updraft (downdraft) region. We generally assume that the vertical motion of the convective drafts dominates their horizontal contributions. Thus, the divergence of the convective mass fluxes reduces to the vertical derivative. The mass fluxes in the updraft and downdraft are governed by the corresponding entrainment and detrainment rates

$$\frac{\partial M_{\mathrm{u,d}}}{\partial z} = \frac{1}{\Delta z} (\epsilon_{\mathrm{u,d}} - \delta_{\mathrm{u,d}}). \qquad (10)$$

Δz is the width of the respective model layer and $\epsilon_{\mathrm{u,d}}$ and $\delta_{\mathrm{u,d}}$ are the integrated entrainment and detrainment rates in this layer. Inserting this relation into Equation (9), we obtain

$$\left. \frac{\partial \rho}{\partial t} \right|_{\mathrm{conv}} = -\frac{1}{A \Delta z} \left(\epsilon_{\mathrm{u}} - \delta_{\mathrm{u}} + \epsilon_{\mathrm{d}} - \delta_{\mathrm{d}} \right). \qquad (11)$$

2.3. Convective transport of heat and moisture constituents

For the convectively active grid columns, the cloud model calculates the following quantities of the updraft and downdraft: the mass flux M, the temperature T, and the specific moisture content q^x.

For simplicity, we here adopt the formulation of the equations and the symbols used in the LM which are given in the LM documentation by DS. We will briefly follow the derivation of the model equations from the averaged primitive equations (cf. DS in their section 3)

DOI: 10.1002/qj

in order to include our convective contributions and thus to determine the additional convective tendencies.

The averaged momentum conservation equation (1) will not be modified, since we do not consider convective momentum transport at this stage. This is subject to future work. The other averaged grid-scale conservation equations, i.e. the conservation of mass (2), the conservation of the moisture components (3), and the conservation of enthalpy (4), are extended to include convective subgrid-scale contributions as described in the following.

Similar to the convective density tendency we obtain the convective tendencies of the required intensive quantities Ψ, i.e. the enthalpy $h = c_p T$ (with c_p the specific heat at constant pressure) and the specific moisture content q^x:

$$\left.\frac{\partial(\rho\Psi)}{\partial t}\right|_{\text{conv}} = -\nabla \cdot \mathbf{J}^{\Psi}_{\text{conv}}$$
$$= -\frac{1}{A\Delta z}\left(\epsilon_{\text{u}}\Psi - \delta_{\text{u}}\Psi_{\text{u}} + \epsilon_{\text{d}}\Psi - \delta_{\text{d}}\Psi_{\text{d}}\right). \quad (12)$$

$\mathbf{J}^{\Psi}_{\text{conv}}$ stands for the convective flux of enthalpy or of the moisture components. For the conversion from flux form into advective form, we split off the temporal density evolution due to convection by discretizing the left-hand side:

$$\left.\frac{\partial(\rho\Psi)}{\partial t}\right|_{\text{conv}} = \frac{\rho^*\Psi^* - \rho(t^n)\Psi(t^n)}{\Delta t}. \quad (13)$$

Quantities at a particular model timestep are denoted by t^n and quantities updated only by the corresponding convective tendencies are marked by asterisks. The updated density ρ^* is given by

$$\rho^* = \rho(t^n) + \Delta t \left.\frac{\partial\rho}{\partial t}\right|_{\text{conv}}, \quad (14)$$

with the convective density tendency from Equation (11). Inserting Equation (13) into Equation (12) yields an expression for Ψ^*. Together with

$$\left.\frac{\partial\Psi}{\partial t}\right|_{\text{conv}} = \frac{\Psi^* - \Psi(t^n)}{\Delta t}, \quad (15)$$

this is used to calculate the convective tendencies:

$$\left.\frac{\partial\Psi}{\partial t}\right|_{\text{conv}} = \left(\frac{\rho(t^n)}{\rho^*} - 1\right)\frac{\Psi(t^n)}{\Delta t}$$
$$- \frac{1}{A\Delta z\rho^*}\left(\epsilon_{\text{u}}\Psi - \delta_{\text{u}}\Psi_{\text{u}} + \epsilon_{\text{d}}\Psi - \delta_{\text{d}}\Psi_{\text{d}}\right). \quad (16)$$

3. Mass lifting experiments

Since the subgrid transport of mass is essential for our convection scheme and represents the actual improvement compared to existing schemes, we analyse some details of its behaviour. The principal feasibility of subgrid mass transport by adding source and sink terms in filtered models (anelastic/Boussinesq) has already been proven in the literature e.g. by Gray *et al.* (1998) and Gray (1999). They used subgrid mass transport as a tool for studying the effect of convection on the large-scale PV field. In our simulations we here are primarily interested in the dynamics of the nearer environment (several ten kilometers) and therefore we neglect the Coriolis force.

We start with a very idealized experiment to demonstrate the subgrid-scale mass lifting by our scheme and the dynamic reaction of the LM. In a dry and stable background atmosphere (vertical temperature gradient 6 K km^{-1}, surface temperature 300 K) without background wind, a single convectively active grid column is initialized in the middle of the model domain.

The model domain comprises 40×40 grid points horizontally with a grid spacing of 0.0625° (≈ 7 km) and 69 vertical levels in 300 m steps. The equidistant level spacing (in contrast to the vertically stretched grid of the operational version of the LM) was chosen to simplify the analysis of gravity waves. Upward-travelling waves are absorbed by a damping layer between 14 000 m altitude and the model top at 20 400 m. Air is entrained, i.e. mass is transfered from the grid to the subgrid scheme, in the lowermost grid box of the active column. The detrainment, i.e. the mass transfer back to the grid, again takes place in a single grid box, which is choosen arbitrarily at 9000 m altitude. The temperature of the detrained air here is set to the local grid-scale temperature to separate forcings from heat and mass transport. Although this adds energy to the lifted air (heating and forced lifting), it simplifies the dynamics of the outflow from the convective cell. The energetically correct case will be discussed below.

In experiment (a), the subgrid-scale mass transport is switched on for one hour at a constant mass flux which transports the mass of the lowermost grid box within that time. After some wind oscillations, which will be studied below, the grid-scale inflow and outflow around the active column becomes predominantly horizontal (see Figure 1), since the background atmosphere is statically stable. The dynamical influence of the active column

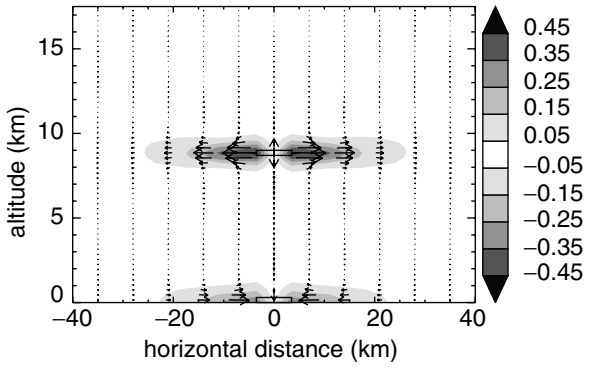

Figure 1. Vertical cross-section through the convectively active grid column and its environment showing the grid-scale wind (arrows) after 30 minutes of mass transport. The grey shading shows the horizontal wind components (ms^{-1}). The entrainment and detrainment regions are marked by black rectangles. For details see text.

DOI: 10.1002/qj

reaches several tens of kilometres horizontally. The vertical extent of the inflow and outflow is restricted to about 1000 m above and below the entrainment and detrainment layer.

The next experiments analyse the production of waves depending on the manner in which the mass transport is switched on and off. In experiments (b) and (c), the mass flux is linearly increased and decreased over 10 minutes at the beginning and the end of the active period instead of an instantaneous switch-on and switch-off. In experiment (c) the detrainment altitude at the beginning of the active period is additionally increased linearly from 750 m to the final value of 9000 m over 10 minutes to qualitatively simulate a vertical growth of the convective cell. Experiments (a), (b), and (c) are compared in Figure 2.

As the temporal development of the vertical wind reveals, the strongest wave disturbance occurs when the mass transport is switched on and off instantaneously (experiment (a)). Chagnon and Bannon (2005) state that a sudden start of convection is not realistic and leads to pressure perturbations which are too high shortly after switch-on. Nevertheless, after about 30 minutes the grid-scale vertical wind becomes stationary with larger values only near the entrainment and detrainment layer. Whereas above the detrainment layer waves essentially radiating from the detrainment layer are visible, the wave pattern below is a combination of waves radiating from both the entrainment and detrainment layer. The upward-travelling component from the switch-on of the entrainment layer becomes visible shortly after switch-off, when a second upward-travelling wave train appears to start from somewhat below the detrainment height (center column in Figure 2). Experiments with a lifted entrainment layer (not shown) confirm that the entrainment layer also radiates waves downwards.

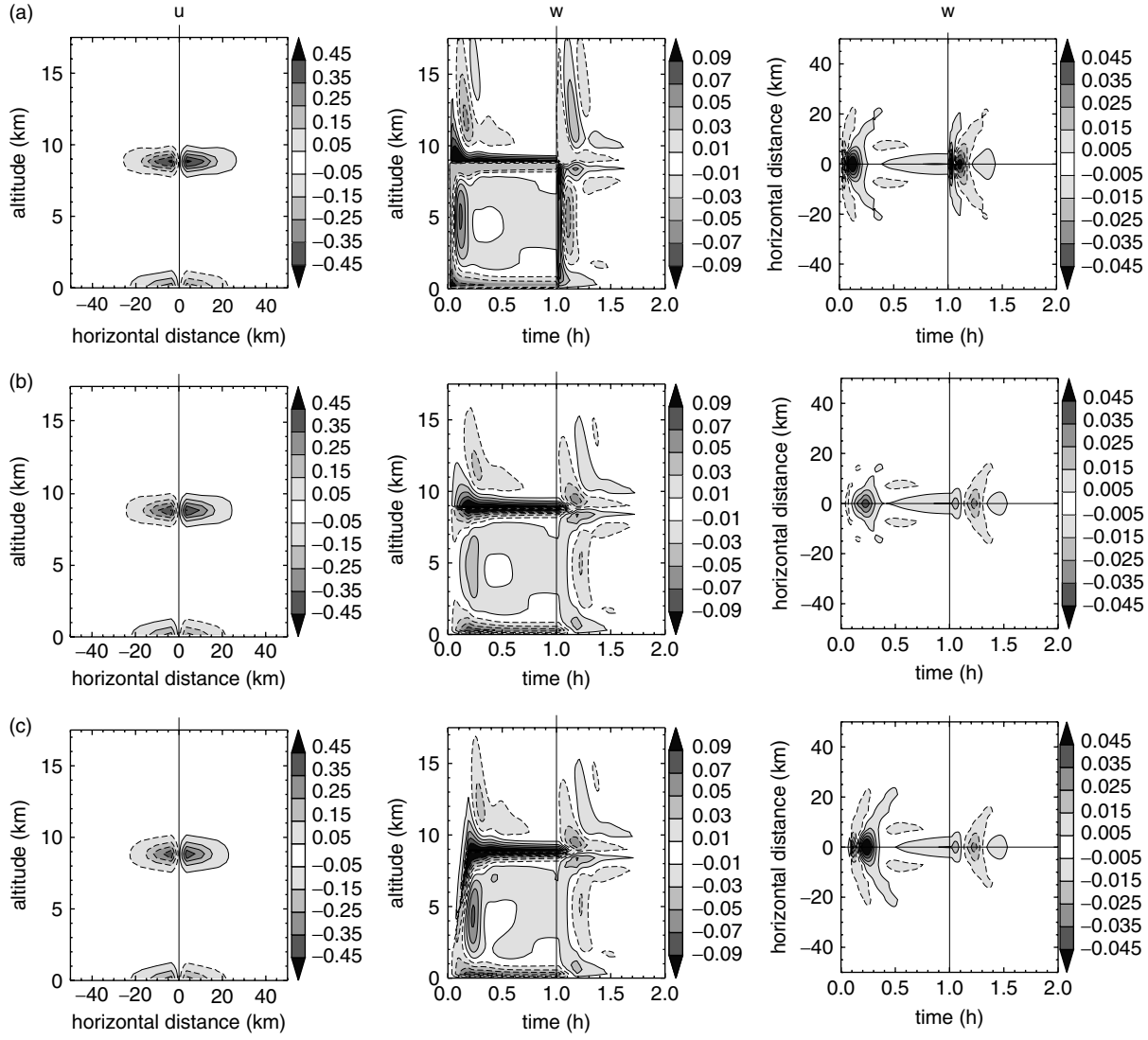

Figure 2. Comparison of experiments (a), (b) and (c): The left column shows vertical cross-sections through the convectively active grid column and its environment showing the grid-scale horizontal wind u after 30 minutes of mass transport, with horizontal distances counted from the location of the active grid column. The centre and right columns show time sequences of the grid-scale vertical wind w through (centre) the convectively active grid column and (right) a horizontal section at 4650 m altitude. The mass transport starts at 0 hours and ends or begins to decrease at 1.0 hours. Units are m s^{-1} for all plots, with contours of negative values dashed. For more details see text.

DOI: 10.1002/qj

The gradual increase/decrease of the mass flux in experiment (b) leads to significantly smaller wave amplitudes than in experiment (a). A sinusoidal change of mass flux with time as proposed by Chagnon and Bannon (2005) leads to results (not shown) similar to the linear case. For our time constant of the mass flux change of 10 minutes, Chagnon and Bannon (2005) found a partitioning of the total energy with 70% accounting for buoyancy waves, almost 30% for the steady state, about 1% for Lamb waves, and practically no acoustic waves.

Experiment (c), with the additional simulation of vertical cell growth, again somewhat increases the wave amplitudes. However, after about 30 minutes, when stationarity has established, the vertical and horizontal wind look very similar for all three experiments. The stationary state of the grid-scale flow is not influenced by details of the switch-on and switch-off of the mass flux.

To analyse the waves in more detail, experiments (a) and (b) with a background vertical temperature gradient of 6 K km^{-1} have been repeated with 4 K km^{-1} and 8 K km^{-1}. The results of experiments (b) are shown in Figure 3. From theory, the switch-on and switch-off of the subgrid mass transport and the resulting grid-scale forcings represent a disturbance of the hydrostatic equilibrium which is transfered to a new equilibrium state by the radiation of gravity waves. This can be confirmed by checking the dispersion relation for the radiated waves.

Figure 3 shows that, as expected, the frequency is higher in the more stable atmosphere than in the more unstable case. This becomes visible when comparing the temporal distances between minima and maxima (i.e. half cycle time) of the vertical wind at a fixed altitude. For the less stable case, e.g. above about 11 km, up to 25% longer cycle times can be found in Figure 3 (middle column). But also below the detrainment height (4650 m altitude, Figure 3 right column), cycle times tend to be longer for the less stable case. In the less stable case the vertical wind amplitudes are somewhat higher, whereas the stationary horizontal wind (after >30 minutes) is significantly stronger in the more stable case. The extent of the dynamical influence is more vertical for weaker static stability and more horizontal for stronger static stability. Between the detrainment and entrainment layer, the grid-scale wind is relatively weak, at least in steady state after the irradiation of gravity waves. This is in contrast to existing convection schemes, which force the whole compensational subsidence down in the local grid box. In the classical schemes this forced subsidence, the strength of which depends on the grid spacing, leads to the stabilizing dry-adiabatic warming. In our scheme there is no such forcing. The only regulation of the subsidence is via the grid-scale (vertical) pressure gradient.

An important issue for our scheme, especially for the later use in a convection parametrization scheme in NWP, is its independence from the grid spacing of the hosting model. To check this, we set up experiment (b) with four different grid spacings of the LM: 28 km, 14 km,

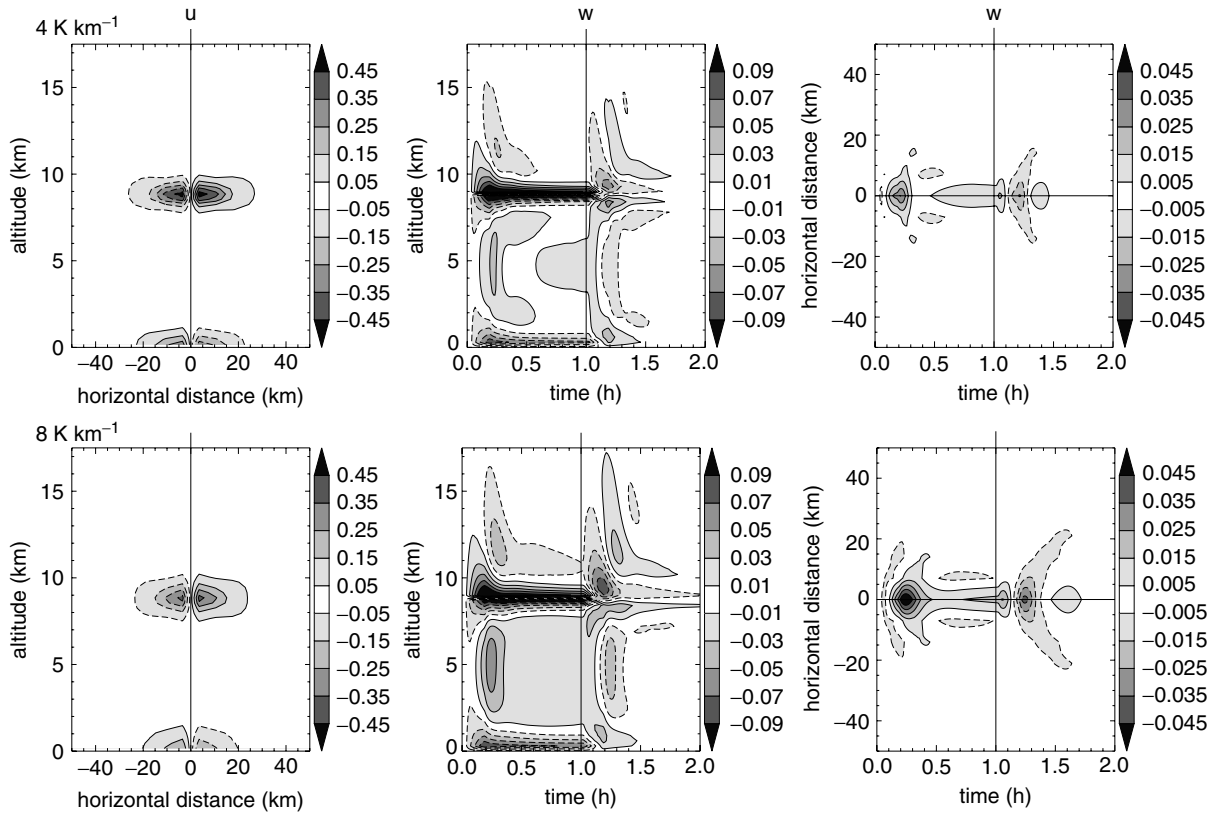

Figure 3. As Figure 2, but for different background vertical temperature gradients: 4 K km^{-1} (upper) and 8 K km^{-1} (lower), all for experiment (c). For 6 K km^{-1}, see lowest row of Figure 2.

DOI: 10.1002/qj

7 km, and 3.5 km. To ensure dynamically comparable situations in all four cases, convectively active cells are now initiated in an area of 56 × 56 km (i.e. 2 × 2, 4 × 4, 8 × 8, and 16 × 16 cells). The total mass flux is the same for all four cases, and thus the mass flux density is the same, what is important for comparable dynamics. The results are shown in Figure 4.

Since the convective area is much larger (56 × 56 km instead of 7 × 7 km) than in experiment (b), we have choosen a somewhat reduced total mass flux here (scaled down by a factor of three) to avoid too strong grid-scale winds due to the very large area of uniform upward transport. Nevertheless, the grid-scale horizontal wind is somewhat stronger than in experiment (b). In all four cases the large-scale structures look very similar although there are apparent differences in the details. To check to what extent these differences are caused by small-scale structures in the high-resolution runs, which geometrically cannot be resolved by the lower-resolution runs, all four output fields of the different runs are averaged onto a 56 × 56 km grid (not shown). After this averaging the horizontal wind fields of the 3.5 km, 7 km, and 14 km runs look practically identical. Only the horizontal wind field of the 28 km run looks slightly smoother. Thus, apparent differences are due only to the grid-scale/subgrid-scale limit deciding which fine structure can be represented on a certain grid. These results confirm that the exchange of mass between the grid-scale equations and the subgrid scheme does not depend on the grid spacing.

For experiment (a) with a background temperature gradient of 6 K km^{-1}, we check the conservation of total mass in the LM. From temperature, pressure and vertical wind we determine the grid-scale mass flux through a horizontal plane at mid-altitude (4.5 km) over the whole model domain. Ideally, the upward subgrid-scale mass flux (from the convection scheme) and the downward grid-scale mass flux integrated over the whole convective period exactly cancel out. In the LM the upper boundary which contains a wave-damping sponge layer (cf. DS) can cause a mass deficit; with the model configuration with 69 layers (model top height at 20 700 m) and a sponge layer above 14 000 m, the difference between the integrated subgrid-scale and grid-scale mass flux is 2.1%, which is unacceptably high. If the model is vertically extended to 79 layers (model top height at 23 700 m) with a sponge layer above 20 000 m, the integrated subgrid-scale and grid-scale mass flux only differ by about 0.1%. This identifies the sponge layer as a cause of mass generation/destruction. However, the transport of mass by our convection scheme and the mass exchange with the grid-scale equations is accurate within reasonable limits which confirms our concept of subgrid-scale mass transport.

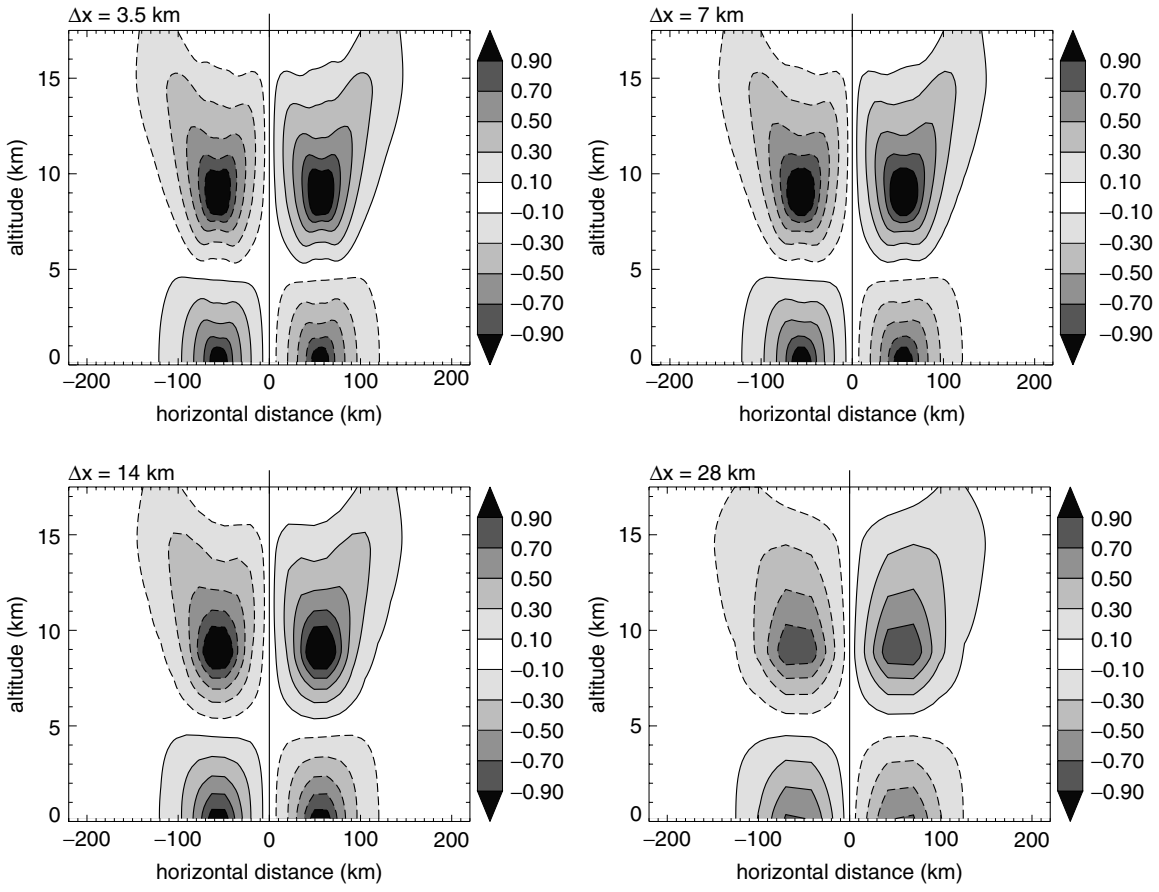

Figure 4. Vertical cross-sections through the convectively active grid column and its environment showing the grid-scale horizontal wind u after 30 minutes of mass transport for different grid spacings as indicated. Contours of negative values are dashed. Units are m s^{-1} for all plots.

DOI: 10.1002/qj

4. Moist convection experiment

To simulate moist convection, we have set up a simple cloud model which calculates the thermodynamics of a convective updraft. The generation of precipitation and a downdraft will be discussed in a subsequent paper. Since this cloud model here is not the focus of our work but a tool to drive our subgrid transport scheme of mass, heat and moisture, we have adopted many features from existing cloud models in the literature.

In the updraft source layer (USL), environmental air is collected to form the updraft by continuous entrainment. As in Bechtold *et al*. (2001), we collect the updraft air from a 60 hPa deep mixed layer, which here is situated at the ground. When the calculation proceeds upwards, at every vertical level a saturation adjustment is performed, such that dry or moist adiabatic ascents are chosen automatically. The saturation adjustment includes a gradual glaciation of the cloud droplets between $-5\,^{\circ}\mathrm{C}$ and $-25\,^{\circ}\mathrm{C}$ (with sinusoidal temperature dependency). The updraft air becomes saturated at the lifting condensation level (LCL) which denotes the cloud base. At the level of free convection (LFC), buoyancy becomes positive and accelerates the updraft up to the equilibrium temperature level (ETL). With negative buoyancy above the ETL, the updraft reaches the cloud top level (CTL), where the kinetic energy is exhausted and the updraft air is detrained to the environment again.

To describe the thermodynamic properties of the updraft air, we use the liquid water static energy h_{il} (e.g. Emanuel, 1994), which is extended by a term considering the ice phase (Bechtold *et al*., 2001). We formulate h_{il} with the specific moisture quantities which are also used in the LM, instead of the mixing ratios:

$$h_{\mathrm{il}} = c_p T + gz - l_{\mathrm{lv}} q^{\mathrm{l}} - l_{\mathrm{iv}} q^{\mathrm{i}}. \tag{17}$$

Here, l_{lv} and l_{iv} are the latent heats of vaporization and sublimation.

Under the assumption that convective transports are predominantly vertical, the continuity equation for the updraft fluxes can be formulated as in Equation (10). For the intensive quantities $\Psi = q^{\mathrm{v}}$, q^{l}, q^{i}, and h:

$$\frac{\partial (M_{\mathrm{u}} \Psi_{\mathrm{u}})}{\partial z} = \frac{1}{\Delta z} (\epsilon_{\mathrm{u}} \Psi - \delta_{\mathrm{u}} \Psi_{\mathrm{u}}). \tag{18}$$

The entrainment and detrainment rates are determined from a buoyancy sorting algorithm proposed by Kain and Fritsch (1990).

As for the sake of simplicity we will again perform our experiments in a homogenous initial atmosphere, convection is forced to start only in a single grid column. The implementation of a physical trigger function will be the subject of future work.

The kinetic energy of the updraft at the LCL is set to an initial value corresponding to a vertical wind of 1 m s^{-1} (Bechtold *et al*., 2001). The kinetic energy increment per level $\Delta E_{\mathrm{kin,u}}$ and the vertical velocity w_{u} of the updraft are computed from the generalized virtual temperature T_{v} (including water loading) similar to Bechtold *et al*. (2001):

$$\Delta E_{\mathrm{kin,u}} = \frac{g}{1+\gamma} \frac{T_{v,\mathrm{u}} - T_{\mathrm{v}}}{T_{\mathrm{v}}} \Delta z, \tag{19}$$

$$w_{\mathrm{u}} = \sqrt{2 E_{\mathrm{kin,u}}}. \tag{20}$$

Here, $\gamma = 0.5$ includes non-hydrostatic pressure perturbations (Kuo and Raymond, 1980). We correct the vertical velocity (and kinetic energy correspondingly) under the assumption that the entrained environmental air has zero vertical momentum:

$$w_{\mathrm{u,corr}} = w_{\mathrm{u}} \frac{M_{\mathrm{u}}}{M_{\mathrm{u}} + \epsilon_{\mathrm{u}}}. \tag{21}$$

The CTL is set at the altitude where the kinetic energy of the updraft is exhausted. At this altitude, all updraft air is detrained to the grid-scale environment. This interactive determination of the CTL and thus of the detrainment height represents a mechanism via which neighbouring convective cells may interact. Together with dynamic interactions via the trigger and closure assumption, this establishes the basis for convective self-organization. However, this discussion is beyond the scope of this introductory paper.

For our moist convection experiment, we initialize the model domain with a conditionally unstable background atmosphere using temperature and moisture profiles from Weisman and Klemp (1982) with the specific water vapour content limited to 12 g kg^{-1} in order to avoid saturation in the boundary layer. This results in a medium value of convective available potential energy (CAPE) of about 1400 m^2 s^{-2}. The initial background wind is set to zero.

Figure 5 shows the temperature and moisture profiles of the updraft and the environment after 30 minutes of convection. The LCL is encountered at about 1500 m altitude. Above the LFC at about 2700 m, buoyancy becomes positive up to the ETL at about 9700 m. The CTL is reached at about 11 500 m altitude. The thermodynamics of the updraft and especially the extent of the convective overshooting beyond the ETL strongly depend on the mixing with the environment; without any entrainment and detrainment the CTL would be situated at about 15 000 m. With doubled mixing, the CTL falls to about 9700 m. Another important point not to be neglected is the consideration of the ice phase; without the latent heat from the glaciation (but with mixing with the environment), the CTL would be found at about 10 600 m. Between about 5000 m and 8000 m altitude, the gradual glaciation of the cloud becomes visible in the conversion of cloud water to ice and the release of latent heat (Figure 5). Above the LCL before glaciation starts and near the CTL the effect of mixing with the (colder) environment shows up as a slight deviation from the moist adiabat.

The vertical distribution of mixing with the environment due to entrainment and detrainment is given in

DOI: 10.1002/qj

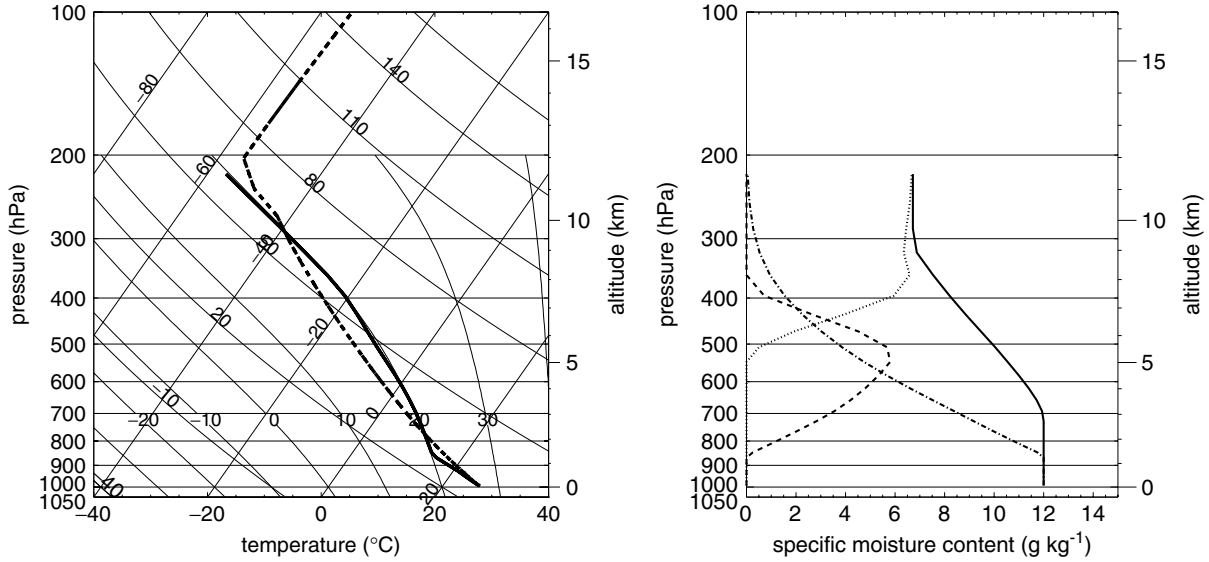

Figure 5. Left: skew$T$–log$p$ plot of updraft temperature (solid) and environmental temperature (dashed). Right: specific water vapour content (dash-dotted), liquid water (dashed), ice (dotted), and total water (solid) in the updraft air.

Figure 6. In the USL (lowermost 60 hPa or 520 m) the updraft mass flux is collected with a constant entrainment rate. Up to the LCL there is no further mixing with the environment. Above the LCL, the buoyancy sorting algorithm (Kain and Fritsch, 1990) is applied. Below the LFC, where buoyancy is negative, detrainment is favoured, whereas above, entrainment leads to a significant increase of the updraft mass flux. Near the ETL, detrainment dominates again. Above the ETL entrainment and detrainment are switched off. Just below the CTL, the whole remaining updraft mass flux is passed back to the grid by detrainment. From the LCL to the CTL the updraft mass flux increases by about 55%, which is within the typical range of 50–70% given by Pielke (1984).

Figure 7 shows the grid-scale wind for the idealized moist convection experiment (cf. Figure 1 for the pure dry mass transport). In contrast to the idealized dry convection experiment (Figure 1), the detrainment height

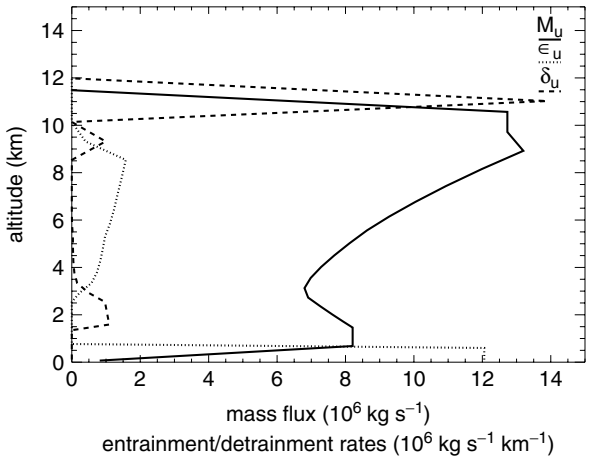

Figure 6. Updraft mass flux (solid), entrainment rate (dotted) and detrainment rate (dashed).

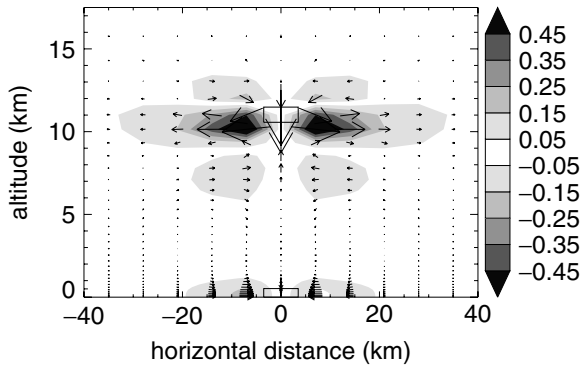

Figure 7. As Figure 1, but for moist convection. For details see text.

here is not arbitrarily prescribed but determined to be energetically consistent by the thermodynamics of the updraft. Due to the convective overshooting beyond the ETL, the detrained updraft air is colder than the environment causing negative buoyancy and grid-scale downward transport. This reaches down to about 1000 m below the detrainment layer. Then the detrained air spreads mainly horizontally as in the idealized dry case. The downward transport also affects the air above the detrainment layer inducing a circulation pattern.

Figure 8 shows the temperature and pressure deviation from the initial atmosphere. The USL pressure is decreased by the local grid-scale mass sink transferring air to the subgrid-scale updraft. In the detrainment layer, pressure is increased by the corresponding local mass source and temperature is decreased, since the detrained updraft air is colder than the environment after the convective overshooting above the ETL. The local downward movement of the air on the grid scale increases the temperature locally by adiabatic heating and increases the pressure down to about 10 km altitude, where the downward movement turns to a horizontal spreading (cf. Figure 7).

DOI: 10.1002/qj

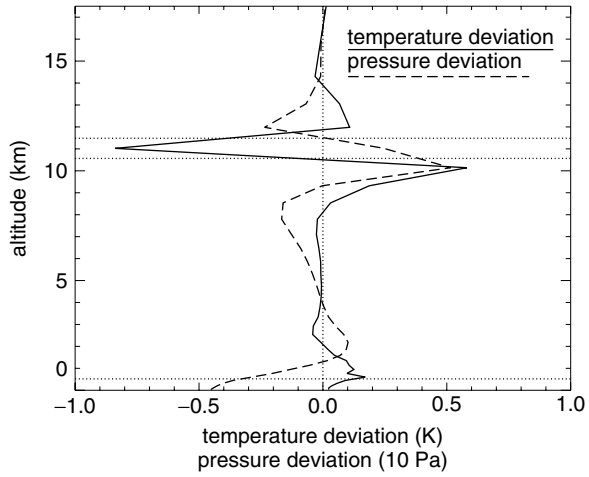

Figure 8. Temperature deviation (solid) and pressure deviation (dashed) from initial atmosphere after 30 minutes of convection. The top of the updraft source layer and the boundaries of the detrainment layer are marked by dotted lines.

As already described in section 3, the grid-scale response to the convective forcing is dominated by gravity waves. The role of gravity waves concerning the convective adjustment in the environment of a convective cell is analysed in detail e.g. by Bretherton and Smolarkiewicz (1989, hereafter abbreviated BS). In explicitly resolved two-dimensional experiments with a non-hydrostatic anelastic model, the authors initialize a convective cloud in a conditionally unstable atmosphere by transient heating. This creates a buoyancy source which radiates gravity waves. The corresponding vertical wind then forces horizontal inflow and outflow via mass conservation. This is to be compared with the grid-scale dynamics in the convective grid column of our scheme, which in addition to heating also exerts a mass forcing to the environment of the convective cell. In an idealized buoyancy source model (hydrostatic linear gravity wave theory), BS get negative vertical wind (cf. their Figure 6), where buoyancy is positive (i.e. below the ETL), and positive vertical wind, where buoyancy is negative (i.e. above the ETL). Except for the near field (local convective grid column and its direct neighbours), these vertical wind components are also observed in the outflow region near the ETL in our experiment (cf. Figure 7). The ETL is located at about 10 km altitude (see Figure 5, left diagram). In this region around the ETL, where buoyancy decreases with altitude from positive to negative values, we see a strong horizontal outflow away from the convective grid column similar to the experiments of BS. In our moist adiabatic experiment (with full thermodynamics and heat transport in the updraft, this section) the detrainment height, which is identical to the CTL, is at about 12 km altitude. Representing a convective overshooting, the detrained air from the subgrid-scale updraft locally sinks to the ETL at about 10 km altitude on the grid scale and then spreads horizontally. In the case of the pure mass lifting scheme (section 3), this horizontal outflow also coincides with the altitude of the mass divergence from the subgrid-scale updraft detrainment. But as the temperature of this detrained updraft air has been set to the environmental temperature, this is also the altitude of the ETL. The inflow near the ground in the USL is forced by the mass convergence of our convection scheme, but the inflow near the CTL (cf. Figure 7) is again buoyancy induced as in the experiments of BS (cf. their Figure 6).

The gravity wave front, which spreads horizontally originating from the convective cell, separates the convectively unadjusted region from the adjusted region. We determine the velocity of propagation of this boundary from the group velocity c_{model} of the first (negative) maximum of the grid-scale vertical wind (cf. Figure 2, lowermost row and Figure 3).

For the different background vertical temperature gradients we get from our experiment (c) $c_{\mathrm{model}} = 66$ m s^{-1} for 4 K km^{-1}, 46 m s^{-1} for 6 K km^{-1} and 34 m s^{-1} for 8 K km^{-1}. We compare these with the theoretical values using the relation $c_{\mathrm{linear}} = N/m$ of BS for the horizontal group velocity c_{linear} from linear wave theory. Here, N is the Brunt–Väisälä frequency and m is the vertical wave number. Setting the half vertical wavelength of the gravity wave source equal to the vertical distance between entrainment and detrainment level (9 km), we obtain $c_{\mathrm{linear}} = 42$ m s^{-1} for 4 K km^{-1}, 36 m s^{-1} for 6 K km^{-1} and 25 m s^{-1} for 8 K km^{-1}. The values from linear wave theory agree with the values from our experiment within 22–36%. (BS obtained an agreement within about 40% for the corresponding comparison.) As stated by Mapes (1993), the environmental subsidence takes place in propagating gravity wave pulses, which can be confirmed by our experiments. To summarize, our subgrid-scale updraft in conjunction with its local grid-scale environment (especially when the full thermodynamics are included) dynamically behaves similarly to the buoyancy source of BS. The proper representation of the environmental subsidence and the gravity wave response are crucial e.g. for the self-organization of convection (Mapes, 1993), which is an important issue for NWP.

5. Conclusions

We have developed a hybrid mass flux approach to parametrize cumulus convection in nonlinear, non-hydrostatic and fully compressible NWP models. For our studies we have chosen the LM of DWD. In our mass flux scheme only the updraft and downdraft are parametrized and the larger-scale environmental subsidence is treated by the grid-scale equations.

To check the dynamical reaction on the grid scale and the proper exchange of mass between the hosting model and the parametrization scheme, we have set up idealized dry mass lifting experiments (without convective heat transport). Entrainment causes grid-scale convergence and the detrained air, which here is set to the same temperature as the environment, spreads mainly horizontally on the grid. A convective grid column radiates

DOI: 10.1002/qj

gravity waves, when convection starts and ends. Whereas the amplitude of the gravity waves depends on the details of the switch-on/switch-off of convection, the stationary state (after about 30 minutes) does not. Four model runs with different grid spacings (3.5 km to 28 km) confirm that the exchange of mass between the model grid and the parametrization scheme does not depend on the chosen grid spacing.

The damping layer at the upper boundary of the LM can cause a mass deficit; in an idealized dry mass lifting experiment, total mass in a convective circulation cell is conserved to better than 0.1%, but only if the damping layer is shifted to above 20 km.

A simple cloud model for an updraft has been set up to drive the parametrization scheme in a moist convection experiment (with convective heat transport). As the detrained air at the cloud top is colder than the environment, it moves down by about 1 km but then mainly spreads horizontally over several tens of kilometres, again as in the dry case without convective heat transport. The subgrid-scale updraft in conjunction with its local grid-scale environment (especially when the full thermodynamics are included) behaves dynamically in a qualitatively similar fashion to the buoyancy source of BS. This confirms the dominant role of gravity waves in the convective adjustment process. A realistic representation of the environmental subsidence and the gravity wave response are crucial for the self-organization of convection (Mapes, 1993).

In a forthcoming paper, the hybrid mass flux approach is planned to be extended to a full convection parametrization scheme, including also precipitation and a downdraft in the cloud model and a trigger and closure assumption for use in NWP.

Acknowledgements

We thank the Deutscher Wetterdienst for providing the Lokal-Modell. We are also grateful to two anonymous referees for their constructive comments. Our work was funded by grant Bo998/7-1 of the Schwerpunktprogramm 1167 by Deutsche Forschungsgemeinschaft.

Appendix–Transformation to temperature and pressure tendencies

Our mass flux scheme determines convective tendencies of the specific moisture content, density and enthalpy. We here briefly describe the transformation of the convective tendencies of density and enthalpy to the prognostic variables temperature and pressure which are also used in the LM.

We add our convective tendencies of density, specific moisture content, and enthalpy to the corresponding (averaged) grid-scale conservation equations (2)–(4) of the LM. We then closely follow the procedure described in DS: The enthalpy conservation equation (Equation (4); (3.33) of DS) is transformed into the following form as described in DS (cf. their equation (3.36)). For convenience, we omit the averaging symbols here and in the following:

$$\rho c_p \frac{\mathrm{d}T}{\mathrm{d}t} = \frac{\mathrm{d}p}{\mathrm{d}t} + Q_\mathrm{h} + \rho \left.\frac{\partial h}{\partial t}\right|_\mathrm{conv}. \tag{A.1}$$

Here, Q_h denotes the diabatic heating terms. As in DS, the material derivative of the equation of state ((3.35) of DS) is taken. Inserting the mass and moisture conservation equations including the convective tendencies and Equation (A.1), we obtain the following (corresponding to (3.39) of DS):

$$\begin{aligned}\frac{\mathrm{d}p}{\mathrm{d}t} = &-\frac{c_p}{c_\mathrm{v}} p \boldsymbol{\nabla}\cdot\mathbf{v} + \frac{c_p}{c_\mathrm{v}}\frac{p}{\rho}\left.\frac{\partial \rho}{\partial t}\right|_\mathrm{conv} \\ &+ \left(\frac{c_p}{c_\mathrm{v}} - 1\right)\left(Q_\mathrm{h} + \rho \left.\frac{\partial h}{\partial t}\right|_\mathrm{conv}\right) \\ &+ \frac{c_p}{c_\mathrm{v}}(Q_\mathrm{m} + Q_\mathrm{m,conv}).\end{aligned} \tag{A.2}$$

Here, Q_m comprises the moisture source terms with the convective contribution $Q_\mathrm{m,conv}$. Since in the LM the *grid-scale* moisture source terms are neglected in the pressure tendency equation (cf. (3.45) and (3.51) of DS), we do the same concerning the *convective* moisture source terms for consistency reasons. Inserting Equation (A.2) into Equation (A.1) leads to the temperature tendency equation (cf. (3.52) of DS):

$$\begin{aligned}c_p\rho\frac{\mathrm{d}T}{\mathrm{d}t} &= \frac{\mathrm{d}p}{\mathrm{d}t} + Q_\mathrm{h} + \rho\left.\frac{\partial h}{\partial t}\right|_\mathrm{conv} \\ &= -\frac{c_p}{c_\mathrm{v}} p\boldsymbol{\nabla}\cdot\mathbf{v} + \frac{c_p}{c_\mathrm{v}}\frac{p}{\rho}\left.\frac{\partial\rho}{\partial t}\right|_\mathrm{conv} \\ &\quad + \frac{c_p}{c_\mathrm{v}}\left(Q_h + \rho\left.\frac{\partial h}{\partial t}\right|_\mathrm{conv}\right).\end{aligned} \tag{A.3}$$

We now collect the convective terms in Equations (A.2) and (A.3) (cf. (3.51) and (3.52) of DS) and obtain the convective temperature and pressure tendencies:

$$\left.\frac{\partial p}{\partial t}\right|_\mathrm{conv} = \frac{c_p}{c_\mathrm{v}}\frac{p}{\rho}\left.\frac{\partial\rho}{\partial t}\right|_\mathrm{conv} + \left(\frac{c_p}{c_\mathrm{v}} - 1\right)\rho\left.\frac{\partial h}{\partial t}\right|_\mathrm{conv}, \tag{A.4}$$

$$\left.\frac{\partial T}{\partial t}\right|_\mathrm{conv} = \frac{1}{c_\mathrm{v}}\frac{p}{\rho^2}\left.\frac{\partial\rho}{\partial t}\right|_\mathrm{conv} + \frac{1}{c_\mathrm{v}}\left.\frac{\partial h}{\partial t}\right|_\mathrm{conv}. \tag{A.5}$$

References

Arakawa A, Schubert WH. 1974. Interaction of a cumulus cloud ensemble with the large scale environment: Part I. *J. Atmos. Sci.* **31**: 674–701.

Bechtold P, Bazile E, Guichard F, Mascard P, Richard E. 2001. A mass flux convection scheme for regional and global models. *Q. J. R. Meteorol. Soc.* **127**: 869–886.

Betts AK. 1986. A new convective adjustment scheme. I: Observational and theoretical basis. *Q. J. R. Meteorol. Soc.* **112**: 677–692.

Bretherton CS, Smolarkiewicz PK. 1989. Gravity waves, compensating subsidence and detrainment around cumulus clouds. *J. Atmos. Sci.* **46**: 740–759.

Bryan GH, Wyngaard JC, Fritsch JM. 2003. Resolution requirements for the simulation of deep moist convection. *Mon. Weather Rev.* **131**: 2394–2416.

Chagnon JM, Bannon PR. 2005. Adjustment to injection of mass, momentum, and heat in a compressible atmosphere. *J. Atmos. Sci.* **62**: 2749–2769.

Charney J, Eliassen A. 1964. On the growth of the hurricane depression. *J. Atmos. Sci.* **21**: 75–81.

Doms G, Schättler U. 2002. *A description of the nonhydrostatic regional model LM. Part I: Dynamics and Numerics.* Consortium for small-scale modelling, Deutscher Wetterdienst, Offenbach, Germany. Available at www.cosmo-model.org.

Emanuel KA. 1994. *Atmospheric convection.* Oxford University Press: New York, USA.

Fritsch JM, Chappell CF. 1980. Numerical prediction of convectively driven mesoscale pressure systems. Part I: Convective parameterizations. *J. Atmos. Sci.* **37**: 1722–1733.

Gray MEB. 1999. An investigation into convectively generated potential vorticity anomalies using a mass forcing model. *Q. J. R. Meteorol. Soc.* **125**: 1589–1605.

Gray MEB, Shutts GJ, Craig GC. 1998. The role of mass transfer in describing the dynamics of mesoscale convective systems. *Q. J. R. Meteorol. Soc.* **124**: 1183–1207.

Gregory D, Rowntree PR. 1990. A mass flux convection scheme with representation of cloud ensemble characteristics and stability-dependent closure. *Mon. Weather Rev.* **118**: 1483–1506.

Kain JS. 2003. The Kain–Fritsch convective parameterization: An update. *J. Appl. Meteorol.* **43**: 170–181.

Kain JS, Fritsch JM. 1990. A one-dimensional entraining/detraining plume model and its application in convective parameterization. *J. Atmos. Sci.* **47**: 2784–2802.

Kain JS, Fritsch JM. 1993. Convective parameterization for mesoscale models: The Kain–Fritsch scheme. *Meteorol. Monographs* **24**: 165–170.

Kuo HL. 1965. On formation and intensification of tropical cyclones through latent heat release by cumulus convection. *J. Atmos. Sci.* **22**: 40–63.

Kuo HL, Raymond, WH. 1980. A quasi-one-dimensional cumulus cloud model and parameterization of cumulus heating and mixing effects. *Mon. Weather Rev.* **108**: 991–1009.

Kurihara Y. 1973. A scheme for moist convective adjustment. *Mon. Weather Rev.* **101**: 547–553.

Manabe S, Strickler RF. 1964. Thermal equilibrium of the atmosphere with a convective adjustment. *J. Atmos. Sci.* **21**: 361–385.

Manabe S, Smagorinski J, Strickler RF. 1965. Simulated climatology of a general circulation model with a hydrological cycle. *Mon. Weather Rev.* **93**: 769–798.

Mapes BE. 1993. Gregarious tropical convection. *J. Atmos. Sci.* **50**: 2026–2037.

Mapes BE. 2003. An information-based approach to convective closure. Research report 93: 89–96. Bureau of Meteorology Research Centre, Melbourne, Australia.

Molinari J. 1993. An overview of cumulus parameterization in mesoscale models. *Meteorol. Monographs* **24**: 155–158.

Pielke RA. 1984. *Mesoscale meteorological modeling.* Academic Press: Orlando, USA.

Shutts GJ. 1994. The adjustment of a rotating, stratified fluid subject to localized sources of mass. *Q. J. R. Meteorol. Soc.* **120**: 361–386.

Tiedtke M. 1989. A comprehensive mass flux scheme for cumulus parameterization in large scale models. *Mon. Weather Rev.* **117**: 1779–1800.

Weisman ML, Klemp JB. 1982. The dependence of numerically simulated convective storms on vertical wind shear and buoyancy. *Mon. Weather Rev.* **110**: 504–520.

Weisman ML, Skamarock WC, Klemp JB. 1997. The resolution dependence of explicitly modeled convective systems. *Mon. Weather Rev.* **125**: 527–548.

DOI: 10.1002/qj